Inorg. Chem. **2008**, *47*, 9813−9827

Solid-State Changes in Ligand-to-Metal Charge-Transfer Spectra of $(NH_3)_5Ru^{III}$(2,4-dihydroxybenzoate) and $(NH_3)_5Ru^{III}$(xanthine) Chromophores

Karsten Krogh-Jespersen,*,† Robert T. Stibrany,† Elizabeth John,† John D. Westbrook,† Thomas J. Emge,† Michael J. Clarke,‡ Joseph A. Potenza,*,† and Harvey J. Schugar*,†

Department of Chemistry and Chemical Biology, Rutgers, The State University of New Jersey, New Brunswick, New Jersey 08903, and Department of Chemistry, Boston College, Chestnut Hill, Massachusetts 02167

Received March 20, 2008

Five distorted-octahedral complexes containing $(NH_3)_5Ru^{III}L$ ions, where L = 2,4-dihydroxybenzoate or a xanthine, have been studied using a combination of X-ray crystallography, solution and polarized single-crystal electronic absorption spectroscopy, and first principles electronic structure computational techniques. Both yellow (**2**) and red (**3**) forms of the complex $(NH_3)_5Ru^{III}L$, where L = 2,4-dihydroxybenzoate, as well as three xanthine complexes in which L = hypoxanthine-κN^7(**4**), 7-methylhypoxanthine-κN^9(**5**), and 1,3,9-trimethylxanthine-κN^7(**6**) were examined. In the solid state, some of these complexes exhibit split low-energy ligand-to-metal charge-transfer (LMCT) bands. Traditional solid-state effects, such as ligand $\pi-\pi$ overlap or hydrogen bonding that might lead to splitting of electronic absorption bands, were probed in an attempt to identify the origins of these unusual observations. For comparison, companion studies were carried out for spectroscopically normal reference complexes of the same ligands. Time-dependent density-functional theory (TD-DFT) calculations, employing modified B3LYP-type functionals with increased contributions of exact exchange, attribute the color change in the crystalline complexes **2** and **3** to π(ligand) → Ru[d(π)] LMCT bands which, in the red form (**3**), arise from ligand donor π-orbitals split by strongly overlapping phenyl moieties in centrosymmetric $(NH_3)_5Ru^{III}$(2,4-dihydroxybenzoate) dimers. Complex **5** does not show split visible absorptions, whereas both the polarizations and energies of the split visible absorptions shown by **4** and **6** also suggest assignment as LMCT. No support is found for relating the split absorptions of **4** and **6** to the details of $\pi-\pi$ xanthine overlap in the solid state; indeed, complex **4** enjoys considerably *less* π-stacking overlap than does **5**. We feel compelled to attribute the split absorptions in crystalline **4** and **6** to the emergence of a LMCT transition originating in the carbonyl lone pair, potentially deriving intensity from the significant intramolecular N−H···O hydrogen bonding present in both **4** and **6** (but not in **5**). The electronic structure calculations suggest an O(n) → Ru[d(σ^*)] LMCT transition; however, this novel assignment must be considered tentative.

Introduction

We report here novel differences between the solution and single-crystal ligand-to-metal charge-transfer (LMCT) absorptions shown by pentammineRu(III) ions complexed to 2,4-dihydroxybenzoate or one of several xanthine ligands. This study extends our long-time interest in the LMCT spectra of Cu(II) and Ru(III) complexes of biologically relevant ligands.[1−3] Although Ru(III) does not play a prominent role in natural metallo-biochemistry, there are promising ruthenium metallopharmaceuticals in clinical trials,[4] and the LMCT spectra of Ru(III) complexes can serve as instructive analogues to those of related Cu(II) chro-

* To whom correspondence should be addressed. E-mail: krogh@rutchem.rutgers.edu (K.K.-J.), potenza@rutchem.rutgers.edu (J.A.P.), schugar@rutchem.rutgers.edu (H.J.S.).
† Rutgers University.
‡ Boston College.

(1) Stibrany, R. T.; Fikar, R.; Brader, M.; Potenza, M. N.; Potenza, J. A.; Schugar, H. J. *Inorg. Chem.* **2002**, *41*, 5203–5015.
(2) (a) Krogh-Jespersen, K.; Zhang, X.; Westbrook, J. D.; Fikar, R.; Nayak, K.; Kwik, W. L.; Potenza, J. A.; Schugar, H. J. *J. Am. Chem. Soc.* **1989**, *111*, 4082–4091. (b) Krogh-Jespersen, K.; Westbrook, J. D.; Potenza, J. A.; Schugar, H. J. *J. Am. Chem. Soc.* **1987**, *109*, 7025–7031; and references cited therein.
(3) Kastner, M. E.; Coffey, K. F.; Clarke, M. J.; Edmonds, S. E.; Eriks, K. *J. Am. Chem. Soc.* **1981**, *103*, 5747–5752.
(4) Clarke, M. J. *Coord. Chem. Rev.* **2003**, *236*, 207–231.

10.1021/ic800511g CCC: $40.75
Published on Web 10/07/2008

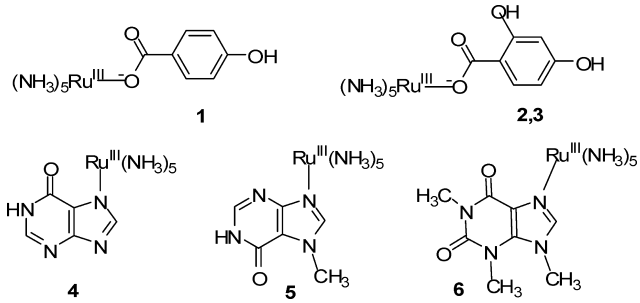

Figure 1. Schematic structures of the cations in **1**−**6**.

mophores.[2] Moreover, the excited states of Ru(II) and Cu(I) complexes involved in metal-to-ligand charge transfer (MLCT) also show useful similarities, which are being explored for solar cell applications.[5,6] Ru(III) and Cu(II) ions share the features of being relatively strong oxidizing species, each with a single d-vacancy that allows relatively low-energy LMCT absorptions to occur from upper occupied ligand orbitals. Ruthenium complexes are well suited for spectroscopic studies owing to their kinetic non-lability and photophysical properties, which have been used to probe long-range electron transfer in biological systems[7−10] and for sensitizing dyes in solar cells.[11,12]

Some time ago, Stritar and Taube studied the electron-transfer and spectroscopic properties of a number of pentammineRu^{III}-carboxylate complexes.[13] The $[(NH_3)_5Ru^{III}$(4-hydroxybenzoate)] complex (**1**) showed a low-energy absorption band at approximately 400 nm, which was absent in the spectra of the parent benzoate or aliphatic carboxylate complexes. This absorption band was intensified and red-shifted to 500 nm for the deprotonated phenolate analogue, thus supporting a LMCT assignment. To explore this type of LMCT in more detail, we have studied related complexes containing $(NH_3)_5Ru^{III}$ units (Figure 1). Both yellow (**2**) and red (**3**) forms of crystals containing the [(pentammineRu^{III})2,4-dihydroxybenzoate] unit have been characterized. These crystals afford identical solution LMCT spectra but show striking differences in their solid-state LMCT absorptions. Equally striking solid-state effects on LMCT absorptions are also shown by [(hypoxanthine-κN^7)$(NH_3)_5Ru]\cdot 3Cl\cdot H_2O$ (**4**)[3] and [(1,3,9-trimethylxanthine-κN^7)$(NH_3)_5Ru]\cdot[ZnCl_4]\cdot Cl$ (**6**), but not by [(7-methylhypoxanthine-κN^9)$(NH_3)_5Ru]\cdot 3Cl$ (**5**).[3] In contrast to complexes **4** and **6**, strong intramolecular hydrogen bonding between the $(NH_3)_5Ru^{III}$ unit and the xanthine carbonyl group is absent in complex **5**. These curious phase-dependent features of LMCT spectra are the subject of the structural, solution, and polarized single-crystal spectroscopic and computational studies reported here.

Experimental Section

Preparation of the Complexes. $[(NH_3)_5Ru^{III}$(2,4-dihydroxybenzoate)]$\cdot SO_4\cdot 0.5(CH_3)_2NCHO$ (2) and $[(NH_3)_5Ru^{III}$(2,4-dihydroxybenzoate)]$\cdot SO_4\cdot 2H_2O$ (3) were prepared by following, with minor variations, a published procedure for related complexes.[13]

$[(NH_3)_5Ru^{III}$(2,4-dihydroxybenzoate)]$\cdot SO_4\cdot 0.5(CH_3)_2NCHO$ (2). A mixture of 0.44 g (1.5 mmol) $[(NH_3)_5RuCl]C1_2$ in 4 mL of H_2O was stirred with 0.66 g (3.0 mmol) of CF_3CO_2Ag for 15 min and filtered to remove the precipitated ionic chloride. The yellow filtrate was added to a stirred mixture of 0.92 g (6 mmol) of 2,4-dihydroxybenzoic acid, 0.11 g (2.8 mmol) of NaOH, 4 g of H_2O, 2 g of dimethylformamide, and a small amount of freshly prepared Zn(Hg) amalgam. A red-orange color developed rapidly, and the mixture was filtered after 5 min. An additional gram of dimethylformamide was added to the filtrate, which then was transferred to a small beaker. Saturated aqueous $(NH_4)_2SO_4$ was layered under the red-orange solution. During overnight refrigeration, a yellow-orange solid formed at the interface. A pipet was used to remove the bottom layer; the solid was collected by filtration, twice suspended in several milliliters of absolute ethanol, filtered, and dried in air. The unoptimized yield of crude **2** was 0.44 g (62%); additional product could have been isolated from the red-orange filtrate.

Yellow, plate-like crystals of **2** were deposited after a filtered solution of 80 mg of the crude material in 6 g of H_2O, 0.4 g of dimethylformamide, and 0.1 g of acetonitrile was allowed to evaporate partially in air at room temperature. The crystals exhibited light-yellow to dark-yellow dichroism when viewed under a polarizing microscope. X-ray analysis (see below) showed these crystals to have the composition **2**. The combination of microscopic examination and density measurement (1.786 g/mL calcd, 1.75(1) g/mL measured by flotation in a mixture of heptane and 1,2-dibromoethane) suggested that the recrystallized product was a pure single phase.

Red six-sided plates of **3** deposited after filtered aqueous solutions of recrystallized **2** were evaporated to dryness in air at room temperature. Depending upon the thickness of the crystals, a red-orange or pale-red/almost-colorless dichroism was observed. The composition of this single phase was determined by X-ray crystallography and density measurement (1.848 g/mL calcd, 1.86(1) g/mL observed by flotation in a mixture of heptane and 1,2-dibromoethane).

$[(NH_3)_5Ru^{III}$(Hypoxanthine-κN^7)]$Cl_3\cdot 3H_2O$ (4) and $[(NH_3)_5Ru^{III}$(7-Methylhypoxanthine-κN^9)]Cl_3 (5). $[(NH_3)_5Ru^{III}$(Hypoxanthine-κN^7)]$Cl_3\cdot 3H_2O$ and $[(NH_3)_5Ru^{III}$(7-Methylhypoxanthine-κN^9)]Cl_3 were prepared by following a published procedure[3] and characterized for single-crystal spectroscopic studies as noted below.

$[(NH_3)_5Ru^{III}$(1,3,9-trimethylxanthine-κN^7)]$\cdot[ZnCl_4]\cdot Cl$ (6). $[(NH_3)_5Ru^{III}$(1,3,9-trimethylxanthine-κN^7)]$\cdot[ZnCl_4]\cdot Cl$ was prepared by variation of a published procedure that afforded the trichloride salt.[14]

A small amount of freshly prepared zinc amalgam, 75 mg of $[Ru(NH_3)_5Cl]Cl_2$ (0.26 mmol), 57 mg of CF_3CO_2Ag (0.26 mmol), and 50 mg of 1,3,9-trimethylxanthine (0.26 mmol) were added sequentially to 20 mL of distilled, deionized water, which had previously been acidified to pH 4 with HCl and degassed under

(5) Armaroli, N. *Chem. Soc. Rev.* **2001**, *30*, 113–124.
(6) Scaltrito, D. V.; Thompson, D. W.; O'Callaghan, J. A.; Meyer, G. J. *Coord. Chem. Rev.* **2000**, *208*, 243–266.
(7) Wishart, J. F.; Zhang, X.; Isied, S. S.; Potenza, J. A.; Schugar, H. J. *Inorg. Chem.* **1992**, *31*, 3179–3181.
(8) Distefano, A. J.; Wishart, J. F.; Isied, S. S. *Coord. Chem. Rev.* **2005**, *249*, 507–516; and references cited therein.
(9) Gray, H. B.; Winkler, J. R. *Q. Rev. Biophys.* **2003**, *36*, 341–372.
(10) Chang, I.-J.; Lee, J. C.; Winkler, J. R.; Gray, H. B. *Proc. Natl. Acad. Sci. U.S.A.* **2003**, *100*, 3838–3840.
(11) Polo, A. S.; Itokazu, M. K.; Murakami I, N. Y. *Coord. Chem. Rev.* **2004**, *248*, 1343–1361.
(12) Klein, C.; Nazeeruddin, M. K.; Di Censo, D.; Liska, P.; Grätzel, M. *Inorg. Chem.* **2004**, *43*, 4216–4226.
(13) Stritar, J. A.; Taube, H. *Inorg. Chem.* **1969**, *8*, 2281–2292.
(14) Clarke, M. J.; Taube, H. *J. Am. Chem. Soc.* **1975**, *97*, 1397–1403.

argon. The mixture was stirred under continued argon purge for 30 min. Following filtration, air was bubbled through the green filtrate for 30 min, during which time the color changed to cherry red. This solution was concentrated to 10 mL, and the pH was adjusted to 2.5 with HCl. The solution was transferred to a beaker and placed in a closed jar containing absolute ethanol. After several days at room temperature, vapor diffusion of the ethanol resulted in the deposition of dichroic red plates as the major phase, along with some elongated purple prisms and small, yellow rhomboids. These three air-stable phases could be separated manually. The dichroic red plates are the subject of the structural and spectroscopic studies described below. Their bulk density, 2.01(1) g/mL, was determined by flotation in a mixture of carbon tetrachloride and 1,2,3-tribromopropane.

Spectroscopic Measurements. Electronic-spectral measurements were made using a computer-interfaced spectrophotometer, built by Aviv Associates, that utilizes a Cary Model 14 monochromator and cell compartment. Low-temperature (80 K) spectra were measured using an Air Products optical Dewar. Polarization measurements of **3**, **4**, and **5** were made using separate polarizers in the sample and reference beams. Matched Glan-Thompson prisms having a usable angular field of approximately 15° were rotated in unison by a chain drive mechanism. Projections of electronic vectors for the single-crystal spectra onto the molecular electronic axes of the ruthenium chromophores were calculated from $\mathbf{P}(\mathbf{u}||\mathbf{h}) = \mathbf{u} - (\mathbf{h}\cdot\mathbf{u})\mathbf{h}/(\mathbf{h}\cdot\mathbf{h})$, where **P** is the projection, **u** is the desired crystallographic vector, and **h** is the vector normal to the desired plane.[15] Electronic spectra were processed and deconvoluted using the Grams/AI software package.

A plate-like crystal of the "red" complex (**3**), 0.013 mm thick, was placed on a quartz flat and masked with black electrical tape. Microscopic examination was used to ensure the absence of light leaks around the masked crystal. Orientation of the unit-cell axes was established by X-ray diffractometry. The **bc** crystal face, the only one that was prominently developed, was oriented perpendicular to the light beam of the spectrophotometer, which was directed along the **a*** reciprocal cell axis. Maximum (red) and minimum (pale-yellow) absorbances of the visible bands were observed with the electric vector of light oriented along the **c** and **b** axes, respectively. These axial vectors also are optical extinction directions imposed by the symmetry of the monoclinic cell. Polarization studies along these directions are free from wavelength-dependent dispersion effects.

Similarly, crystals of **4** (0.026 mm thick plate), **5** (0.011 mm thick plate), and **6** (0.050 mm thick plate) were examined using a diffractometer to verify their unit cells and orientations. The prominent **ab** face of **4** showed orange/yellow dichroism, whereas that of **5** showed a yellow/colorless dichroism; **6** exhibited a red/yellow dichroism. Maximum and minimum absorbances of the absorption(s) shown by both **4** and **5** were observed with the light beam of the spectrophotometer directed along the **c** axis, and with the electric vector of the light oriented, respectively, parallel to **a** and parallel to **b.** The **a** and **b** axes also are optical extinction directions for orthorhombic cells. For **6**, the light was directed along the **c** axis, but the maximum absorbance (red color) occurred with the electric vector parallel to **b**, and the minimum absorbance (yellow color) occurred with the electric vector parallel to **a**. Single-crystal spectra of **2** were not measured. The space group for crystals of **2**, *P*1, does not impose any symmetry constraints on dispersion effects with the result that extinction directions are wavelength dependent, making the interpretation of polarized spectra difficult.

(15) Sands, D. E. In *Vectors and Tensors in Crystallography*; Dover Publications, Inc.: Mineola, NY, 1995; p 45.

Table 1. Crystallographic Data for Structures **2**, **3**, and **6**

	2	**3**	**6**
formula	$C_{17}H_{47}N_{11}O_{17}Ru_2S_2$	$C_7H_{24}N_5O_{10}RuS$	$C_8H_{25}Cl_5N_9O_2RuZn$
Fw	943.92	471.44	623.06
a, Å	7.2458(5)	15.4850(8)	7.4212(3)
b, Å	9.6065(6)	7.6969(4)	8.8688(3)
c, Å	12.8376(8)	14.9386(8)	31.3964(12)
α, deg	80.3290(10)	90.	90.
β, deg	88.7540(10)	107.845(1)	90.
γ, deg	85.5150(10)	90.	90.
V, Å^3	877.47(10)	1694.82(15)	2066.42(13)
space group	*P*1	$P2_1/c$	$P2_12_12_1$
Z	1	4	4
ρ_{calc}, g/cm^3	1.786	1.848	2.003
ρ_{obs}, g/cm^3	1.75(1)	1.86(1)	2.01(1)
μ, mm^{-1}	1.06	1.10	13.53
trans factor	0.83−1.00	0.88−1.00	0.38−1.00
T, K	100(2)	200(2)	100(2)
data/restraints/parameters used in refinement	9269/3/448	5144/6/274	3194/317/245
largest peak, hole, e/Å^3	3.43, −1.18	0.949, −0.482	2.392, −2.938
R_F[a] R_{wF}[2b]	0.040, 0.104	0.031, 0.072	0.079, 0.185

[a] $R_F = \sum||F_o| - |F_c||/\sum|F_o|$; selection criterion $I > 2\sigma(I)$. [b] $R_{wF}{}^2 = \{[\sum[w(|F_o{}^2 - F_c{}^2|)/\sum[w(F_o{}^2)]]\}^{1/2}$; selection criterion all $F_o{}^2$.

X-ray Diffraction Studies. Diffraction measurements for **2**, **3**, and **6** were made with a Bruker SMART CCD area detector system diffractometer using ϕ and ω scans. For **2** and **3**, monochromated Mo Kα radiation, $\lambda = 0.71073$ Å, was used; for **6,** data were collected using monochromated Cu Kα radiation, $\lambda = 1.54178$ Å. In all cases, data were collected over all of reciprocal space, and to a resolution of 0.70 Å for **2** and **3**, and of 0.84 Å for **6**. Cell parameters were determined using the SMART software.[16a] The SAINT package[16a] was used for integration of data, Lorentz, polarization, and decay corrections, and for merging data. Absorption corrections were applied using SADABS.[16b]

Structures were solved and refined on F^2 using the SHELX system and all data.[16c,d] Partial structures were obtained by direct methods; the remaining non-hydrogen atoms in each structure were located using difference Fourier techniques. H atoms were located on difference Fourier maps or placed at calculated positions. For H atoms whose thermal parameters were not refined, isotropic temperature factors were set equal to 1.2−1.5 U_N, where N is the atom bonded to H. Views of the structures were prepared using ORTEP32 for Windows.[17a,b] Crystal data and additional details of the data collection and refinement for the three crystals studied here are given in Table 1, and as Supporting Information.

Each of the three structures proved to be non-routine in some way. Attempts to solve the structure of triclinic **2** in the space group $P\bar{1}$ with a disordered DMF solvate molecule were unproductive, and the structure was solved and refined smoothly in space group *P*1 with two cations, two anions, and the DMF solvate molecule as the asymmetric unit/unit cell. Inspection of the correlation matrix revealed a number of relatively large correlation coefficients arising from the near centrosymmetric relationship of the two unique

(16) (a) *SHELXTL (Version 6.10), Saint-Plus (Version 6.02), and SMART (WNT2000 Version 5.622)*; Bruker AXS Inc.: Madison, WI, 2000. (b) Blessing, R. H. *Acta Crystallogr.* **1995**, *A51*, 33–38. (c) Sheldrick, G. M. *SHELXS-97. Acta Crystallogr.* **1990**, *A46*, 467–473. (d) Sheldrick, G. M. *SHELXL-97. A Computer Program for the Refinement of Crystal Structures*; University of Göttingen: Göttingen, Germany.

(17) (a) Farrugia, L. J. *J. Appl. Crystallogr.* **1997**, *30*, 565. (b) Burnett, M. N.; Johnson, C. K. *ORTEPIII*, Report ORNL-6895; Oak Ridge National Laboratory, Tennessee, U.S.A., 1996. (c) *Crystal Structure Refinement, IUCr Texts on Crystallography 8*; Müller, P., Ed.; Oxford University Press: Oxford, England, 2006; p 126.

cations. In the structure of **3**, the sulfate anion exhibited a positional disorder about one of its triad axes; as a consequence, three of the oxygen atoms were split and were placed on partially occupied sites. Crystals of **3**, obtained from different batches over a period of years, all exhibited this disorder. The salt **6** crystallized in the chiral space group $P2_12_12_1$ and could only be refined successfully as a racemic twin. Such refinement necessitated the introduction of a large number of distance and thermal constraints to facilitate convergence, a procedure that is not uncommon for crystals with this type of twinning.[17c]

Computational Details. All the computational data presented here are based on calculations using density-functional theory (DFT)[18] methods as implemented in the GAUSSIAN03 series of computer programs.[19] A relativistic, 28e effective core potential (ECP) and corresponding valence basis set (8s7p6d/[6s5p3d]) were used for the Ru atom (SDD model);[20] the second-row elements C, N, and O carried all-electron, full double-ζ plus polarization function basis sets (D95(d));[21] and hydrogen atoms were assigned a double-ζ 21G basis set.[22] Calculations of electronic ground-state properties made use of the standard three-parameter hybrid exchange functional of Becke[23] (B3) and the correlation functional of Lee, Yang, and Parr (LYP).[24] Geometries of monomeric $(NH_3)_5RuL^+$ (L = deprotonated *p*-hydroxybenzoate; deprotonated 2,4-dihydroxybenzoate), $(NH_3)_5RuL^{2+}$ (L = acetate; benzoate; *p*-hydroxybenzoate; 2,4-dihydroxybenzoate) and $(NH_3)_5RuL^{3+}$ (L = hypoxanthine-κN^7; 7-methylhypoxanthine-κN^9; 1,3,9-trimethylxanthine-κN^7) species, a dimeric $(NH_3)_{10}Ru_2L_2^{4+}$ (L = 2,4-dihydroxybenzoate) complex, and the free ligands were fully optimized assuming vacuum conditions.

Electronic transition energies and intensities (oscillator strengths, *f*) were calculated using the time-dependent DFT (TD-DFT) formalism[25] and the ECP/basis sets just described. Assignment of a particular electronic transition ($\pi \rightarrow \pi^*$, $\pi \rightarrow$ d LMCT, etc.) was based on consideration of the magnitude of the oscillator strength, the largest transition amplitude(s) for the excitation, and by visualization of the contributing MOs. The experimental spectra were measured in a condensed phase (aqueous solution or a mull) and to facilitate comparisons of computed and experimental transition energies electrostatic effects of the polar medium should be incorporated into the TD-DFT wave functions. This was accomplished via the self-consistent polarizable conductor model (CPCM),[26] always choosing water as the "solvent".

Furthermore, we found the conventional B3LYP combination of functionals to be suitable for excited-state calculations only on the neutral organic ligands and on metal complexes carrying a net +3 charge. For the calculations on metal complexes featuring smaller net charge, it was necessary to make computational adjustments to trace analogous electronic transitions through the various complexes. With the B3LYP functionals, the transition energies become too low (sometimes by more than 0.5 eV) in the complexes which contain negatively charged ligands. Applying non-hybrid functionals worsened the situation, in some cases making the transition energies appear negative. Rather than introducing a number of correction factors, we decided to increase the fractional contribution of Hartree−Fock (exact) exchange in the hybrid exchange functional above the 20% value prescribed in the B3 functional.[23] The tendency for DFT to underestimate the band gap for weakly interacting systems, and hence for TD-DFT to underestimate the electronic excitation energies, when local, time-independent functionals are employed is well documented.[27] Increasing the contribution of Hartree−Fock exchange to the overall exchange functional increases the orbital energy separation between the occupied and the unoccupied levels and thus increases the computed transition energies, including the energies of the charge-transfer states of interest here. The molecular orbitals and hence configurations that contribute to a particular transition are not significantly altered by this procedure; neither are the computed intensities. A crude survey using $(NH_3)_5RuL^{2+}$ (L = acetate, benzoate) as test molecules indicated that a combination of 40% Hartree−Fock exchange (and hence 60% Slater local exchange) was more suitable for calculations on excited states of metal complexes with a net +2 charge, that is, the $(NH_3)_5Ru^{III}$−L complexes which contain a ligand carrying a single negative charge (e.g., L = *p*-hydroxybenzoate; 2,4-dihydroxybenzoate). The 40/60 fractional mix of Hartree−Fock/Slater exchange appeared to be appropriate for excited states of the dimeric complex (overall +4 net charge) as well. For $(NH_3)_5Ru^{III}$−L complexes containing a ligand with a net charge of −2 (e.g., L = deprotonated *p*-hydroxybenzoate or deprotonated 2,4-dihydroxybenzoate), we found that a 50/50 mix of Hartree−Fock/Slater exchange worked well.

Results and Discussion

Crystal Structures of 2, 3, and 6. The structures of **2** and **3** each contain $[(NH_3)_5Ru^{III}DHB^-]^{2+}$ cations (DHB^- = 2,4-dihydroxybenzoate), sulfate anions, and either 0.5 dimethylformamide (DMF) molecules (**2**) or two water molecules (**3**), respectively, per asymmetric unit. Structure **6** contains $[(NH_3)_5Ru^{III}TMX]^{3+}$ cations (TMX = 1,3,9-trimethylxanthine), and both tetrachlorozincate and chloride anions in equal amounts. Views of the four unique cations in the three structures are shown in Figure 2, while Figure 3 shows a general Cartesian coordinate system useful for describing these and related structures, and for interpreting the electronic spectra of their crystals. In each structure, five $N(NH_3)$ atoms and an O(carboxylate) atom from DHB^- or an N(imine) atom from TMX complete a distorted octahedron about Ru. The largest deviations from octahedral symmetry in structures **2** and **3** (Table 2) are associated with the DHB^- ligands, as evidenced by the N(ax)−Ru−X(ligand) and N(eq)−Ru−X(ligand) angles, both of which, on average, deviate substantially (ca. 5°) from their ideal values of 180° and 90°, respectively (the magnitude of the deviations can be seen from the standard deviations in the averages reported in Table 2). Using the same angular measures, structure **6** exhibits more nearly a regular octahedral coordination geometry than does **2** or **3**.

(18) Parr, R. G.; Yang, W. In *Density-Functional Theory of Atoms and Molecules*; University Press: Oxford, 1989.
(19) *Gaussian 03, Revision B.03*: Frisch, M. J.; et al. Gaussian, Inc.: Pittsburgh, PA, 2003; see Reference 1 in the Supporting Information for the complete reference to Gaussian 03.
(20) Becke, A. D. *J. Chem. Phys.* **1993**, *98*, 5648–5652.
(21) Lee, C.; Yang, W.; Parr, R. G. *Phys. Rev. B* **1988**, *37*, 785–789.
(22) Andrae, D.; Häussermann, U.; Dolg, M.; Stoll, H.; Preuss, H. *Theor. Chim. Acta* **1990**, *77*, 123–141.
(23) Dunning, T. H.; Hay, P. J. In *Modern Theoretical Chemistry*; Schaefer, H. F., Ed.; Plenum: New York, 1976; pp 1−28.
(24) Binkley, J. S.; Pople, J. A.; Hehre, W. J. *J. Am. Chem. Soc.* **1980**, *102*, 939–947.
(25) Casida, M. E.; Jamorski, C.; Casida, K. C.; Salahub, D. R. *J. Chem. Phys.* **1998**, *108*, 4439–4449.
(26) Cossi, M.; Rega, N.; Scalmani, G.; Barone, V. *J. Comput. Chem.* **2003**, *24*, 669–681.
(27) (a) See, for example, Tozer, D. J. *J. Chem. Phys.* **2003**, *119*, 12697–12699. (b) Dreuw, A.; Weisman, J. L.; Head-Gordon, M. *J. Chem. Phys.* **2003**, *119*, 2943–2946. (c) Perdew, J. P. *Int. J. Quant. Chem., Quant. Chem. Symp.* **1986**, *19*, 497–523.

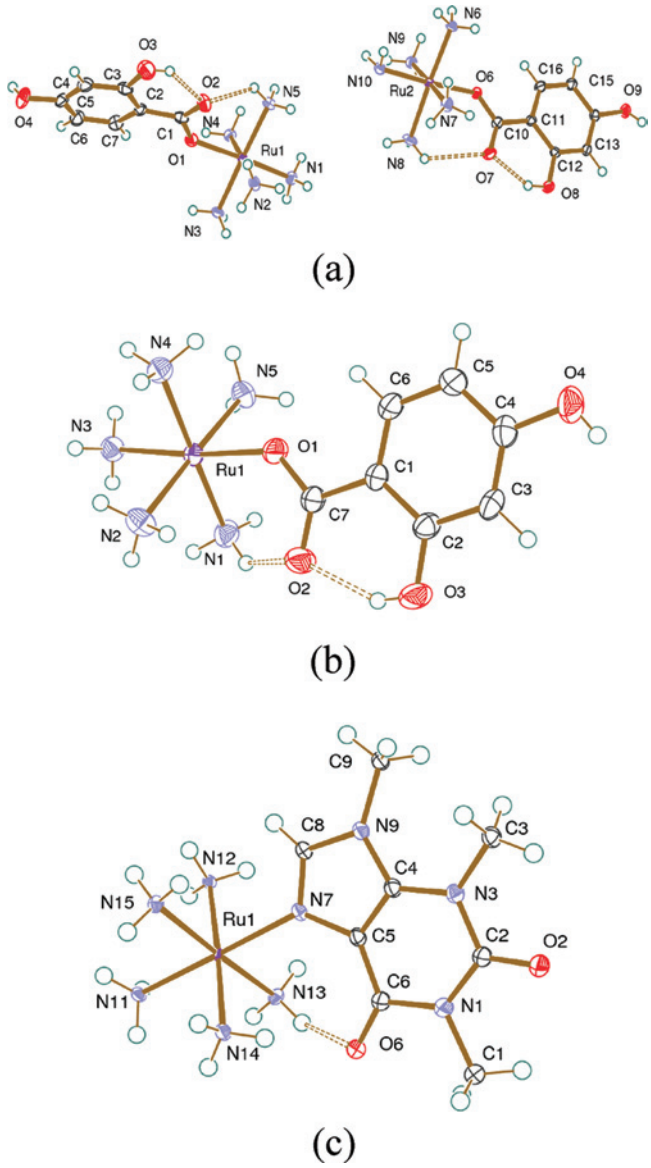

Figure 2. Structures of the cations in **2** (a), **3** (b), and **6** (c) showing the atom numbering schemes. Dashed lines indicate intramolecular hydrogen bonds. Thermal ellipsoids are shown at the 30% probability level.

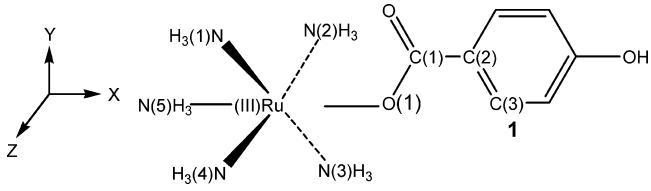

Figure 3. General coordinate system used for species **1**−**7**. The plane of the organic ligand defines the *xy* plane; the N atoms of the four "equatorial" ammine ligands define the *yz* plane. "Equatorial" ammine ligands are numbered 1−4, while the "axial" ammine ligand is numbered 5.

Mean axial and equatorial Ru−N bond lengths in **2** and **3** are equal to within ± 0.01 Å, and appear to be marginally shorter than those in **6**.

Except for a 2−4° phenyl/carboxylate twist in the cations of **2** and **3**, as indicated by the torsion angles in Table 2, the DHB^- and TMX ligands are planar and are oriented such that the plane of the ligand is staggered with respect to the ammine groups (Figure 4). The planes of the ligands do not bisect the N(ax)−Ru−N(ax) angles exactly; rather, they are canted 5−10° from the bisector toward certain axial ammine ligands, as indicated by the N(2)−Ru−X(2)−C(1) torsion angles in Table 2. For this geometry, the π systems of the DHB^- and TMX ligands have an appropriate orientation and symmetry to interact strongly with the singly occupied $Ru(d_{xz})$ orbital (Figure 3). An ammine N−H group in each of the cations in **2**, **3**, and **6** forms an intraionic hydrogen bond to an oxygen atom of the DHB^- or TMX ligand (Table 2), the location of which (Figure 4) is consistent with the direction of canting noted above. Additionally, the cations in **2** and **3** each form intraionic O(carboxylate)···H−O(hydroxyl) hydrogen bonds (Figure 2).

In structures **2** and **3**, the several species in the lattices are linked by an extensive hydrogen-bond network involving each of the ammine groups, all of the O(sulfate) atoms, both solvate water molecules in the case of **3**, and the O(aldehyde) atom from the DMF solvate molecule in **2**. Structure **6** contains no *anions* capable of forming strong hydrogen bonds. Consequently, in addition to the intraionic hydrogen bonds shown in Table 2, the *cation* in **6** forms a single, interionic N(13)−H···O(2) hydrogen bond, as well as several weaker hydrogen bonds, to the chloride and $ZnCl_4^{2-}$ anions. Details of these hydrogen-bonding networks for **2**, **3**, and **6** are given as Supporting Information.

Packing diagrams for **2**, **3**, and **6** are shown in Figure 5. The structure of **2** contains layers of alternating $(NH_3)_5Ru^{III}DHB^-$ cations and sulfate anions along the **c** cell direction. In the layers near the planes $x = 0$ and $x = {}^1/_2$, the two unique cations, one in each layer, are approximately perpendicular to each other. The DMF solvate molecules are located near the corners of the unit cell outline. Intercation distances suggest little, if any, $\pi-\pi$ bonding among the cations. Crystals of **3** contain layers of alternating sulfate ions and water molecules centered about the $x = 0$ plane, separated by layers containing pairs of centrosymmetrically related $(NH_3)_5Ru^{III}DHB^-$ cations stacked head-to-tail and centered about the plane $x = {}^1/_2$. In this arrangement, the ammines, water molecules, and sulfate anions form a "hydrophilic" layer with extensive hydrogen bonding. The overlapping, substituted-phenyl rings are coplanar with an interplanar separation of 3.596(3) Å, and, within a given dimer, 12 C(phenyl)···C(phenyl) interionic distances in the range 3.760(4) Å to 3.786(3) Å, all slightly shorter than the value of 3.8 Å typically associated with $\pi-\pi$ bonding.[28] We conclude that there is extensive $\pi-\pi$ overlap in **3**, but essentially none in **2**. In **6**, layers along the **c** cell direction containing cations, chloride, and $ZnCl_4^{2-}$ ions centered about the plane $x = {}^1/_4$ alternate with layers of cations, $ZnCl_4^{2-}$, and chloride ions centered about the plane $x = {}^3/_4$; there is no indication of $\pi-\pi$ stacking among the cations.

Many of the structural features of **2** and **3** reported here, including the slight deviations from octahedral symmetry of the $(NH_3)_5Ru^{III}$ units, the staggered orientation of the DHB^- and TMX ligands with respect to the equatorial ammines, and the existence of intraionic N−H···X(ligand) hydrogen

(28) Janiak, C. J. *J. Chem. Soc., Dalton Trans.* **2000**, *3885*, 3896.

Table 2. Metric Parameters for Structures **2**, **3**, and **6** (Å, deg)

	2		**3**		**6**	
			Distances			
Ru−N(ax)[a]	2.091(17)	$N = 2$[b]	2.0840(19)	$N = 1$	2.104(10)	$N = 1$
Ru−N(eq)	2.106(9)	$N = 8$	2.104(5)	$N = 4$	2.124(8)	$N = 1$
Ru−X(ligand)[c]	2.023(5)	$N = 2$	2.0039(16)	$N = 1$	2.094(11)	$N = 1$
			Angles			
cis-N(eq)−Ru−N(eq)	90.0(13)	$N = 8$	90.0(19)	$N = 4$	90.1(30)	$N = 4$
trans-N(eq)−Ru−N(eq)	178.2(6)	$N = 4$	179.0(10)	$N = 2$	177.4(4)	$N = 2$
N(ax)−Ru−N(eq)	90.0(23)	$N = 8$	90.3(12)	$N = 4$	89.7(17)	$N = 4$
N(eq)−Ru−X(ligand)	90.2(37)	$N = 8$	89.8(46)	$N = 4$	90.3(13)	$N = 4$
N(ax)−Ru−X(ligand)	174.7(22)	$N = 2$	174.37(8)	$N = 1$	179.4(5)	$N = 1$
			Torsion Angles			
N(2)−Ru−O(1)−C(1)[d]	50.7(4), 40.9(4)		52.5(2)		35.1(16)	
Ru−O(1)−C(1)−C(2)	2.5(6), 6.9(6)		−2.7(4)			
O(1)−C(1)−C(2)−C(3)	−4.2(6), −4.1(6)		2.0(4)			

		intramolecular hydrogen bonds			
crystal	H bond	D−H	H···A	D···A	D−H···A
2	O(3)−H···O(2)[e]	0.84	1.91	2.625(5)	142
2	N(5)−H···O(2)	0.91	2.28	2.981(6)	134
2	O(8)−H···O(7)	0.84	1.82	2.563(4)	146
2	N(8)−H···O(7)	0.91	2.43	3.031(6)	124
3	O(3)−H···O(2)	0.80(4)	1.87(4)	2.584(3)	148(4)
3	N(1)−H···O(2)	0.91	2.26	2.976(3)	135
6	N(13)−H···O(6)	0.89	2.27	3.050(17)	146
6	N(14)−H···O(6)	0.89	2.05	2.822(17)	144

[a] Axial (ax) and equatorial (eq) designations correspond, respectively, to atoms N(5), and N(1) through N(4), as shown in Figure 3. [b] Values of *N* refer to the number of entries averaged; for such entries the average value and the standard uncertainty (su) of the mean are reported. [c] X refers to the ligating atom of the DHB$^-$ and TMX ligands; that is, O for structures **2** and **3**, and N for structure **6**. [d] Atom numbering for the torsion angles is as sketched in Figure 3. [e] Atom numbering for the intra-ionic hydrogen bonds is as in Figure 2.

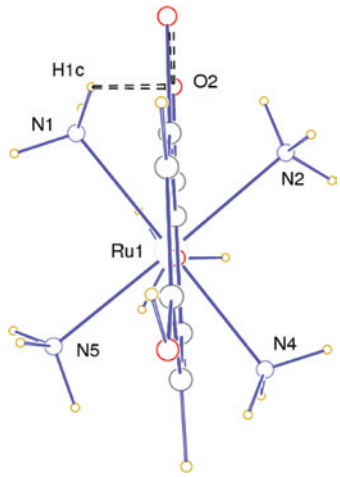

Figure 4. View of the cation in **3** showing the relative orientation of the DHB$^-$ ligand with respect to the equatorial ammine ligands. Dashed lines indicate hydrogen bonds. This relative orientation prevails for structures **1**−**6**.

bonds, when the ligand contains an appropriate acceptor, pertain also to published structures **4** and **5**.[3]

Electronic-Spectral and Computational Studies. PentammineRu^{III}(benzoate) Complexes (1−3). Deconvoluted electronic spectra of **2**, **3**, and the free anion DHB$^-$ are presented in Figure 6 and summarized in Table 3. The pK_a values for the first and second proton ionizations of 2,4-dihydroxybenzoic acid (DHB) are 3.1 and 8.6, respectively.[29] In pH 6.2 phosphate buffer, more than 99% of the free ligand is thus present as DHB$^-$ and the insignificant remainder is present as DHB^{2-}. Deconvolution of the free DHB$^-$ UV-spectrum (Figure 6a) indicates the presence of four intense transitions in the 25,000−50,000 cm^{-1} region; the observed transition energies are in excellent agreement with those calculated for four intensity-carrying $\pi \rightarrow \pi^*$ DHB$^-$ transitions (Table 3). Solutions of **2** (or **3**) at pH 5 (Figure 6b) display, in addition to several of the UV absorptions shown by free DHB$^-$, two additional low-energy absorption bands centered at 23,600 cm^{-1} and 31,200 cm^{-1}, whose origins and striking solid-state polychromism are discussed below.

Neither spin-forbidden nor spin-allowed ligand-field absorptions having molar extinction coefficients much greater than 50 are expected at energies below ∼30,000 cm^{-1} for Ru(III) complexes.[13,30] The first prominent (ε > 500) absorptions of $(NH_3)_6Ru^{3+}$ and $(NH_3)_5Ru(H_2O)^{3+}$ complexes occur at ∼ 36,000 cm^{-1} and have been assigned to LMCT.[13,30] Substitution of the aquo ligand of this latter complex by carboxylate gives rise to one new absorption band with maximum at 34,100 cm^{-1}, assigned as carboxylate → Ru(III) LMCT.[13] In aqueous solution, the maximum of this absorption systematically red-shifts to 33,900 cm^{-1} for acetate and to 33,800 cm^{-1} for benzoate; further to 33,300 cm^{-1} for *p*-hydroxybenzoate (*p*-HB$^-$) and, as noted in Table 3, to 31,200 cm^{-1} for DHB$^-$. The *p*-HB$^-$ complex exhibited additional low energy absorption around 25,000 cm^{-1}, a feature not shown by the acetate or benzoate complexes. In basic solution (pH not reported),[13] the absorption at 25,000 cm^{-1} was significantly red-shifted to 20,000 cm^{-1} and became slightly more intense (ε_{max} > 530). This change was

(29) Martell, A. E.; Smith, R. M. *Critical Stability Constants*, Vol. 5: First Supplement; Plenum Press: New York, NY, 1982; p 345.

(30) (a) Navon, G.; Sutin, N. *Inorg. Chem.* **1974**, *13*, 2159–2164. (b) Meyer, T. J.; Taube, H. *Inorg. Chem.* **1968**, *7*, 2369–2379.

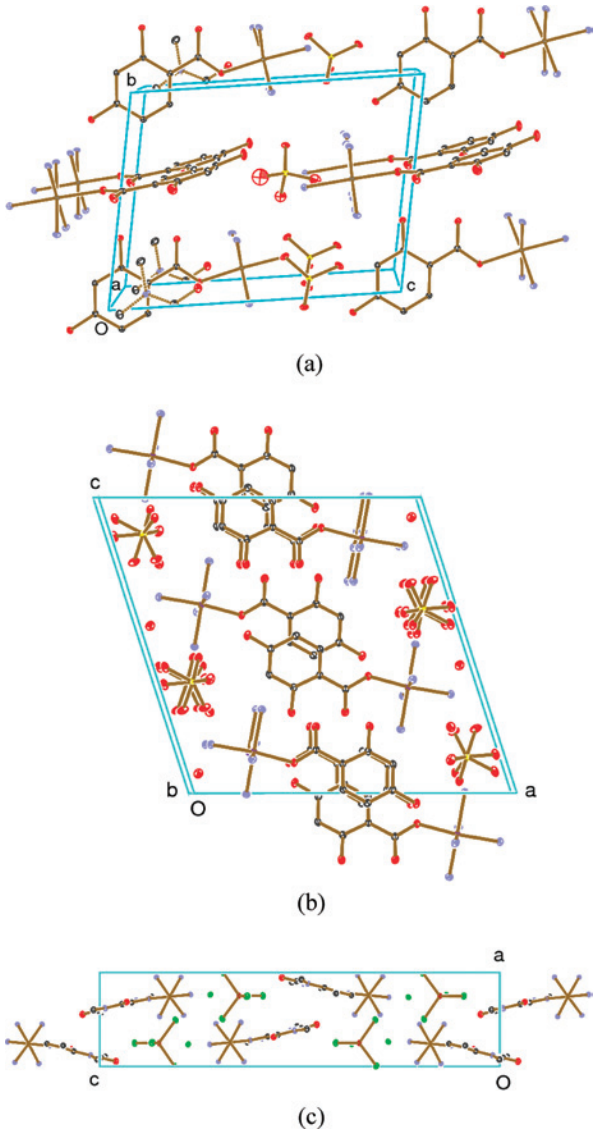

Figure 5. Packing diagrams for **2**, **3**, and **6**. (a) View, approximately perpendicular to (100), of the structure of **2**. (b) Projection, along the **b** axis, of the structure of **3**. (c) Projection, along the **b** axis, of the structure of **6**. For clarity, H atoms have been omitted.

attributed to ionization of the phenolic proton and was reversible. Although not explicitly noted, such spectral behavior implies assignment of the absorption as LMCT, red-shifted relative to the *p*-HB$^-$ complex by the increased electron density of a *p*-HB^{2-} ligand. Finally, the solution spectra of free *p*-HB$^-$ were said to be little changed by complexation to the (NH$_3$)$_5$Ru^{3+} unit of **2**.[13]

The observations noted above strongly imply that the low-energy absorptions displayed by **1** (and analogues) are due to LMCT, and they are confirmed as such by our present TD-DFT calculations. The coordinate system we use for the near-octahedral (NH$_3$)$_5$Ru^{III}−L complexes of interest here is defined in Figure 3: a planar (or nearly planar) organic ligand L is situated in the *xy* plane, approximately bisecting two N−Ru−N angles, and four ammine N atoms define the *yz* plane. Carboxylates and benzoates are strong π-donors, which will preferentially interact with the d_{xz} component of the t_{2g} d(π)-set of orbitals on the central metal ion; hence, the idealized electronic configuration of the ground state Ru^{III} ion becomes $d_{yz}^2 d_{xy}^2 d_{xz}^1$. For the (NH$_3$)$_5$Ru^{III}(acetate) species, we calculate a LMCT transition at 34,800 cm^{-1} (f = 0.011), in very good agreement with the reported absorption (shoulder) at 33,900 cm^{-1}.[13] The transition principally involves excitation of an electron from a π orbital of the acetate unit to the singly occupied Ru(d_{xz}) orbital. The active acetate π orbital is the out-of-phase combination of O($2p_z$) orbitals, polarized so that the contribution to the donor orbital is largest on the O atom bonded to Ru. However, the transition does acquire some (π, π^*) character from a localized acetate excitation at higher energy. In the (NH$_3$)$_5$Ru^{III}(benzoate) species, this low-energy LMCT transition is computed at 31,950 cm^{-1} (f = 0.075) and is described fairly well solely as a single excitation from the out-of-phase combination of acetate O[2p(π)] orbitals, slightly perturbed by a phenyl MO, into the Ru(d_{xz}) orbital.

The electronic-structure calculations for **1** predict π(*p*-HB$^-$) → Ru(d_{xz}) LMCT transitions at 26,400 cm^{-1} (f = 0.057); 32,700 cm^{-1} (f = 0.005), and 34,400 cm^{-1} (f = 0.021) (see Table 3). The *p*-hydroxyl group interacts strongly with one member of the (initially) degenerate π-HOMOs of the phenyl group, shifting it to higher energy. Electron transfer from this perturbed and destabilized phenyl orbital, which also contains a contribution from the carboxylate moiety (viz., benzoate discussed above), into the Ru(d_{xz}) orbital gives rise to the lowest-energy LMCT absorption computed at 26,400 cm^{-1} (observed about 25,000 cm^{-1}). The transition computed at 32,700 cm^{-1} originates in the other high-lying π-orbital of the phenyl group, but it carries little intensity and does not result in an experimentally resolved absorption feature, because the ligand donor orbital does not contain a significant contribution from the carboxylate moiety; thus donor−acceptor overlap is poor. Finally, the transition computed at 34,400 cm^{-1} is the one that is most analogous to the single transitions observed in the (NH$_3$)$_5$Ru^{III}-acetate and benzoate complexes. The two computed transitions at higher energy (32,700 cm^{-1} and 34,400 cm^{-1}) contribute together to the band observed as a shoulder near 33,000 cm^{-1}. Upon ionization of the *p*-hydroxyl group of **1**, the TD-DFT calculations predict the appearance of a low-energy transition at 20,800 cm^{-1} (f = 0.040), clearly assignable as (*p*-HB^{2-}) → Ru(d_{xz}) LMCT, which energetically provides an extremely good match to the red-shifted absorption exhibited by **1** in alkaline solution (∼20,000 cm^{-1}).[13] Thus, the experimental observations made previously by Stritar and Taube strongly implied that the low-energy electronic absorptions exhibited by **1** were due to LMCT, and they are unequivocally confirmed as such by our present calculations.

Relative to *p*-HB$^-$, the additional phenolic OH substituent present in DHB$^-$ increases the electron density in the aromatic ring and further destabilizes the higher lying phenylic π-orbitals. This causes the two observed low-lying absorptions of the homologous DHB$^-$ complexes to red-shift by a few thousand wavenumbers (Table 3, spectra of **2** vs **1**). The calculations predict a somewhat larger (∼ 5,000 cm^{-1}) red-shift to the π(DHB$^-$) → Ru(d_{xz}) LMCT transitions in **2**. The computed transitions are at 21,600 cm^{-1} and 28,400

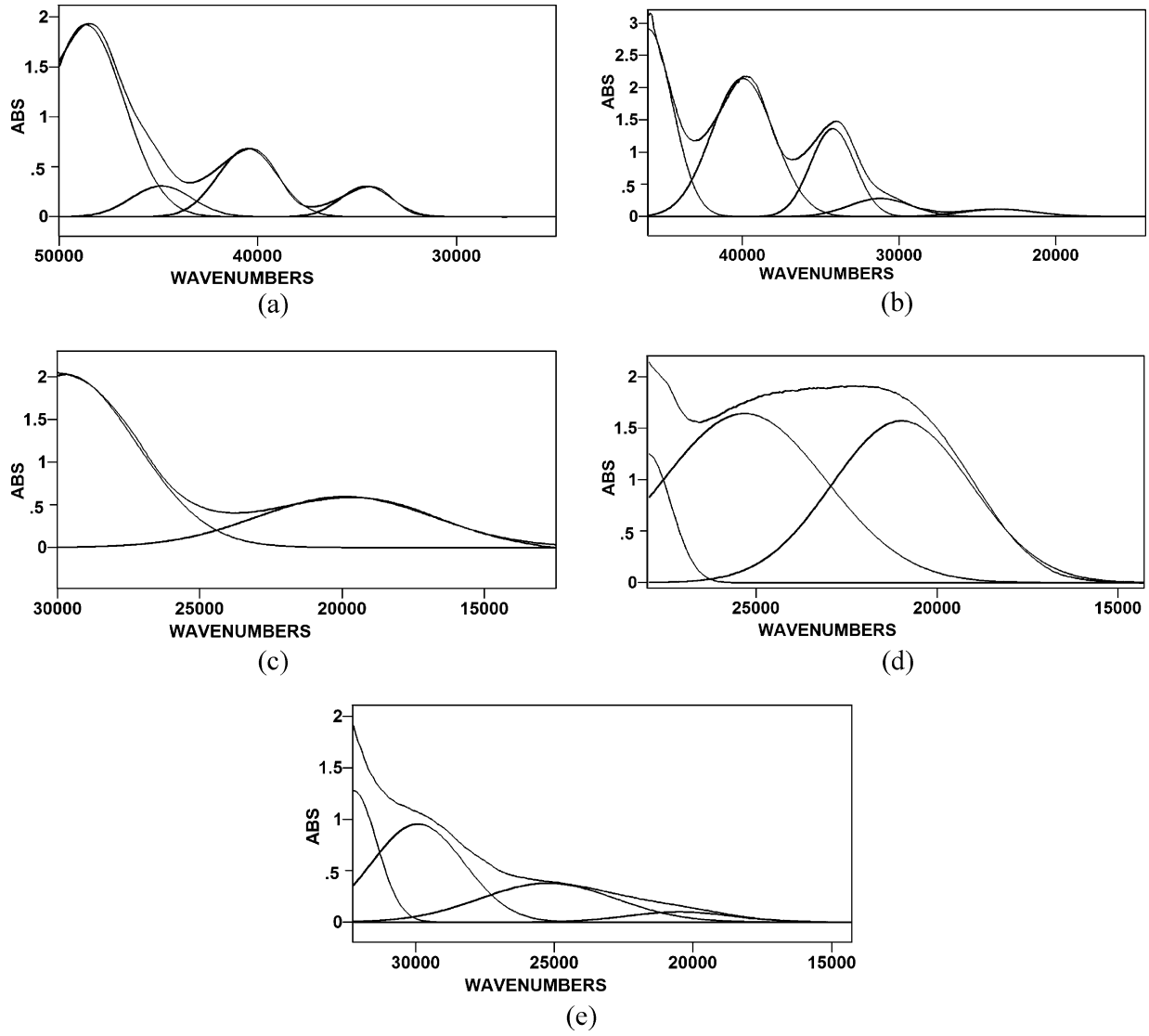

Figure 6. Deconvoluted electronic spectra of (a) 6.72×10^{-4} M DHB^- at room temperature in pH 6.2 phosphate buffer having a path length of 0.1 cm; (b) 2.33×10^{-4} M **2** at room temperature in pH 5 aqueous solution having a path length of 1.0 cm; (c) 6.57×10^{-4} M **2** at room temperature in pH 10 aqueous solution having a path length of 1.0 cm; (d) a polarized spectrum of **3** at room temperature (3.783 M, pure single crystal, 0.013 mm thick) with the electric vector parallel to **c**; and (e) same as (d), but with the electric vector parallel to **b**.

cm^{-1}, whereas the deconvoluted spectrum shows peaks at 23,600 cm^{-1} and 31,200 cm^{-1}. Contour plots of the principal molecular orbitals involved are shown in Figure 7. The transition of low energy originates in a DHB^- (π)-donor orbital, 7(a), and terminates in a Ru[d(π)] acceptor orbital, 7(c). The higher-energy excitation originates in a second DHB^- (π)-donor orbital of lower energy, 7(b), but terminates in the same Ru[d(π)] acceptor orbital, 7(c). Deprotonation of one of the phenolic groups to afford a $(NH_3)_5Ru^{III}(DHB^{2-})$ species additionally destabilizes the ligand π-orbitals with concomitant observed (Figure 6c) and calculated (for deprotonation at the 2-hydroxy site) red-shifts of the LMCT bands by approximately 3,000 cm^{-1} (Table 3). To our knowledge, it has not been established which hydroxy group in DHB^- has the lowest pK_a, and the results from the TD-DFT calculations for species deprotonated at the 2- or the 4-hydroxy site are quite similar.

In the near-octahedral ligand fields associated with the observed site symmetries of **2**−**6** and a strongly π-donating ligand in the xy plane (Figure 3), the d-electron configuration of the Ru(III) ion in a one-electron picture is formally $d_{yz}^2 d_{xy}^2 d_{xz}^1$ (t_{2g}^5). The non-cubic ligand field, combined with spin−orbit coupling effects, causes further modest splitting and mixing of the Ru(III) orbitals.[31,32] Consequently, the formally half-occupied d_{xz} orbital acquires some d_{xy} and d_{yz} character, affording a mixed orbital still having predominantly d_{xz} character but rotated somewhat toward d_{xy} and d_{yz}. The percentage hole character of the Ru(III) d_{xz} orbital could be considerable (perhaps even greater than 50%) for strong π-donor ligands such as DHB^- and purines, that complete the coordination geometries of the strongly π-accepting $(NH_3)_5Ru^{III}$ units present in **2**−**6**.[32] The TD-DFT calculations on **2**−**6** always predict two very low-lying d → d excitations (1,000−3,000 cm^{-1} above the ground state), corresponding to the alternative occupancies of the t_{2g} set of orbitals. For

(31) Kaplan, D.; Navon, G. *J. Phys. Chem.* **1974**, *78*, 700–703.
(32) LaChance-Galang, K. J.; Doan, P. E.; Clarke, M. J.; Rao, U.; Yamano, A.; Hoffman, B. M. *J. Am. Chem. Soc.* **1995**, *117*, 3529–3538.

Table 3. Summary of Observed (Deconvoluted) and Calculated Electronic Spectra for 2,4-Dihydroxybenzoate (DHB$^-$) and Complexes **1**, **2**, and **3**[a,b]

	solution or single crystal			mull	calc. (TD-DFT)		
system	energy	ε_{max}	$\Delta\nu^{1/2}$	energy	energy	f	assignment
DHB$^-$[c]	34,600	4,600	3,000		32,900	0.17	$\pi \rightarrow \pi^*$
	40,500	10,200	3,500		40,600	0.12	$\pi \rightarrow \pi^*$
	44,900	4,600	3,600		45,100	0.38	$\pi \rightarrow \pi^*$
	48,700	28,600	4,500		48,200	0.39	$\pi \rightarrow \pi^*$
1[d]	25,000	530			26,400	0.057	$\pi \rightarrow d_{xz}$ LMCT
	33,000(sh)	2700			32,700	0.005	$\pi \rightarrow d_{xz}$ LMCT
					34,400	0.021	$\pi \rightarrow d_{xz}$ LMCT
1[d,e]	20,000	>530			20,800	0.040	$\pi \rightarrow d_{xz}$ LMCT
2[f]	23,600	500	5,800	~22,000(br)	21,600	0.044	$\pi \rightarrow d_{xz}$ LMCT
	31,200	1,200	4,700		28,400	0.016	$\pi \rightarrow d_{xz}$ LMCT
	34,200	5,900	3,300		36,000	0.121	$\pi \rightarrow \pi^*$
	40,000	9,200	4,700		37,200	0.226	$\pi \rightarrow \pi^*$
	~46,000	12,500	3,600		41,900	0.188	$\pi \rightarrow \pi^*$
2[g]	19,900	900	7,200		18,400	0.058	$\pi \rightarrow d_{xz}$ LMCT
	29,700	1,900	3,800		30,300	0.031	$\pi \rightarrow d_{xz}$ LMCT
	35,200	8,200	5,300		33,400	0.104	$\pi \rightarrow \pi^*$
	41,000	12,000	5,400		33,700	0.178	$\pi \rightarrow \pi^*$
	~46,000	11,000	5,800		43,800	0.055	$\pi \rightarrow \pi^*$
3[h]	21,000	310	4,600	~19,000(br)	19,400	0.074	$\Pi^+ \rightarrow d_{xz}$ LMCT
	25,300	330	5,300		24,000	0.008	$\Pi^- \rightarrow d_{xz}$ LMCT
3[i]	20,200	19	3,900		19,400	0.074	$\Pi^+ \rightarrow d_{xz}$ LMCT
	24,400	65	5,000		24,000	0.008	$\Pi^- \rightarrow d_{xz}$ LMCT
	30,600	220	5,600		34,500	0.042	$\pi \rightarrow d_{xz}$ LMCT
					35,000	0.122	$\pi \rightarrow d_{xz}$ LMCT

[a] Generally, only transitions with a computed oscillator strength (f) larger than 10^{-2} are shown; see Supporting Information for a more complete tabulation. [b] Energies in cm^{-1}; extinction coefficients (ε) in L mol^{-1} cm^{-1}. [c] Measured in pH 6.2 phosphate buffer. [d] Reference.[13] Calculations performed on (NH$_3$)$_5$Ru^{III}(HB^{1-}) [e] Alkaline solution. Calculations performed on (NH$_3$)$_5$Ru^{III}(HB^{2-}) with deprotonation at the 4-hydroxy site [f] Measured in pH 5 aqueous solution. Calculations performed on (NH$_3$)$_5$Ru^{III}(HB^{1-}) [g] Measured in pH 10 aqueous solution. Calculations performed on (NH$_3$)$_5$Ru^{III}(DHB^{2-}) with deprotonation occurring at the 2-hydroxy site [h] Single crystal, electric vector parallel to **c**. [i] Single crystal, electric vector parallel to **b**.

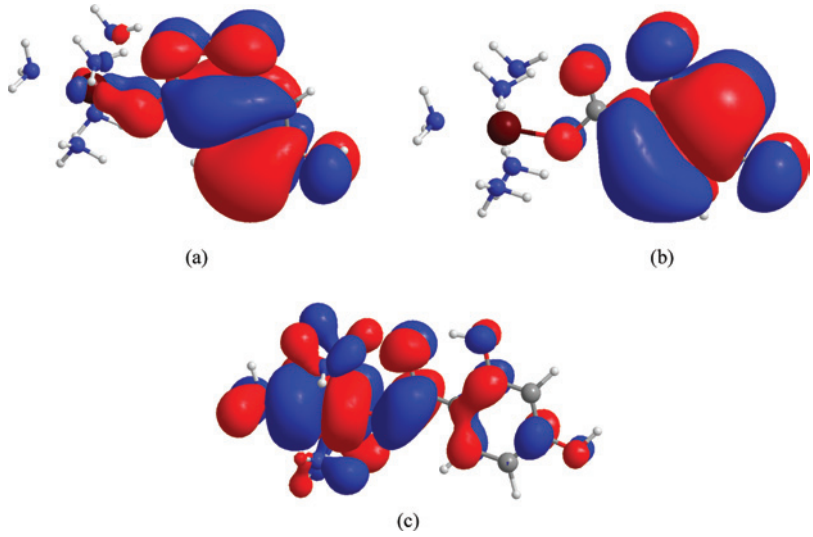

Figure 7. Contour plots of principal orbitals involved in the DHB$^-$(π) → Ru[d(π)] LMCT transitions in **2**. The same isocontour value applies to all three plots. (a) HOMO β spin−orbital, a DHB$^-$ (π)-donor orbital; (b) HOMO-1 β spin−orbital, a second DHB$^-$ (π)-donor orbital; and (c) LUMO β spin−orbital, a Ru[d(π)] acceptor orbital. The transition amplitudes for the elementary excitations HOMO $\beta \rightarrow$ LUMO β and HOMO-1 $\beta \rightarrow$ LUMO β are very large and dominate the overall intensities of the two low-lying ligand-to-metal charge-transfer transitions in **2** (Table 3).

simplicity in band assignments, we will continue to refer to the potentially mixed Ru^{III} d-vacancy as d_{xz}.

The electronic transitions in the aqueous hydroxybenzoate complexes discussed above all appear to be well described as ligand[(π)] → Ru[d_{xz}] LMCT with no particular involvement of Ru(d_{yz}, d_{xy}) orbitals in the final state. Moreover, these transitions should be strongly polarized along the Ru^{III}−L bond direction,[2b] an expectation which mirrors the results of polarized single-crystal spectroscopic studies reported below for complexes **3**−**6**, whose essentially planar DHB$^-$ or purine ligation also share the staggered orientation relative to two of the *cis*-ammine groups located in the "*yz*" plane.

Solid-state spectra of **2** and **3** are expected to show modest red-shifts in LMCT bands relative to those recorded in the solution spectra. Stark-effect studies have revealed substantial changes in dipole moments for the LMCT excitation of Ru(III) complexes.[33] For example, the pyridine → Ru(III) LMCT absorption at 20,300 cm^{-1} shown by (NH$_3$)$_5$Ru^{III}(4-aminopyridine) carries a dipole-moment change of 18 ± 3 D.[32] Because the dipole moment in the ground state of the

$(NH_3)_5Ru^{III}(DHB^-)$ complex must be substantially greater than that of the excited LMCT state, formally a $(NH_3)_5Ru^{II}(DHB)$ species, high-dielectric aqueous media should preferentially stabilize the ground state. Lesser preferential stabilization of the ground state in the lower dielectric solid-state lattice ought to cause a red-shift in the mull LMCT absorptions relative to those shown by the corresponding solution complex. Indeed, the electronic spectra of **2**, measured in mineral-oil mulls (not shown), show the lowest-energy LMCT absorption around ~22,000 cm^{-1}, a red-shift of ~1,600 cm^{-1} relative to the aqueous solution spectra. Also, the mull spectra (not shown) of **3** are *considerably* broader than those of **2** and presumably embody a comparable red-shift. The deconvoluted low-energy absorptions of **3** are split by more than the calculated difference in the absorptions for the two crystallographically unique molecules of **2**, consistent with the relative broadness of the two spectra. Details are given in the following few paragraphs.

Examination of **3** by polarized microscopy revealed a pronounced red/pale-yellow dichroism when the electric vector of light was oriented, respectively, parallel to the **c** and **b** crystal axes. The visible absorptions of the single crystals are significantly broadened relative to those of aqueous **2** or **3** (both afford the same solution complex) and the polycrystalline mull spectra of **2**, whose space group is suboptimal for polarization studies (see Experimental Section). Gaussian deconvolution of the broad visible absorption band in Figure 6d suggests that it is comprised of two equally broad, overlapping bands at ~21,000 cm^{-1} and ~25,000 cm^{-1}, approximately centered about the lowest-energy solution LMCT absorption at 23,600 cm^{-1} (Table 3). Owing to the substantially greater intensity of LMCT absorption at ~31,000 cm^{-1}, an estimate of the intensity of this band in the solid-state spectrum could only be observed in the "pale-yellow" orientation; the optical density for this absorption was too high to measure in the "red" orientation.

For further analysis, the solid-state spectra must be transformed to those obtainable if polarized light could hypothetically be directed along molecular axes. For electric-dipole transitions, band intensities are proportional to the square of the transition moments, which depend upon squares of the projections of the molecular axes along the crystallographic axes (Table 4). For structure **3**, the calculated squares of the Ru−O(DHB^-) bond vector projections along the **b** and **c** axes are 0.0083 and 0.0662, respectively; the major component of the Ru−O projection is 0.9254 along the **a** axis. The Ru−O(DHB^-) bond vector is largely parallel to **a** and nearly orthogonal to **b**, as is apparent from the crystal packing viewed down the **c*** axis (Figure 8a). Unfortunately, the thin, plate-like morphology of **3** did not permit measurement of the polarized spectra along **a**. From the projections, the calculated reduction in *oscillator strength* is 0.0662/0.0083, or 8.0, in fair agreement with an observed decrease in *molar extinction coefficients* of 330/65 ~ 5.1 for the absorption at approximately 25,000 cm^{-1}, but not in accord with the 16-fold (310/19) decrease of the absorption at approximately 21,000 cm^{-1} (Table 3). The large intensity reductions, but not disappearance, of the absorptions when the electric vector was rotated from the **c** to the **b** (Figure 6e) axis indicates that all three absorptions are strongly polarized along the Ru^{III}−O bond, yielding further support to their assignment as LMCT transitions.

Table 4. Squares of the Projection of the $(NH_3)_5Ru$−L Bond Vector on the Crystallographic Axes

compound	axis	projection
3 (L = 2,4-DHB^-)	**a**	0.9254
	b	0.0083
	c	0.0662
4 (L = N(7)-hypoxanthine)	**a**	0.7196
	b	0
	c	0.2804
5 (L = N(9)-7-methylhypoxanthine)	**a**	0.3365
	b	0
	c	0.6635
6 (L = N(7)-1,3,9-trimethylxanthine)	**a**	0.0978
	b	0.8844
	c	0.0178

Could relatively minor structural differences among the monomers be responsible for the spectral variations? As reported above, at the DFT/B3LYP-optimized ground-state geometry, the LMCT band for monomeric $(NH_3)_5Ru^{III}(DHB^-)$ is computed at 21,600 cm^{-1} (f = 0.044). In a monomeric $(NH_3)_5Ru^{III}(DHB^-)$ complex constructed using the crystallographic coordinates for **3**, the lowest-energy LMCT absorption is computed at 22,300 cm^{-1} (f = 0.034). Similarly, considering the two non-equivalent $(NH_3)_5Ru^{III}(DHB^-)$ units in **2** individually as molecular species, we compute the lowest energy LMCT transition at 23,700 cm^{-1} in one unit (Ru-yellow-a, f = 0.038) and at 21,500 cm^{-1} in the other (Ru-yellow-b, f = 0.031). Thus, the spectral changes predicted from slightly different coordination geometries present in various $(NH_3)_5Ru^{III}(DHB^-)$ units are modest. Barring extensive interactions among the units, crystals of **2** would be predicted to show a broad absorption band (centered near (23,700 cm^{-1} + 21,500 cm^{-1})/2 ~ 22,500 cm^{-1}) because of the presence of two molecular units in equal proportions absorbing with similar strengths. Interestingly, the spectrum of **2** in a mull does show broad absorption peaking ~22,000 cm^{-1} (Table 3). In this analysis, the colors of **2** and **3** should be very similar (yellow). This is obviously not the case; however, minor geometric differences among the molecular units cannot be responsible for the red-shifted LMCT band observed in crystalline **3**.

Differences in dielectric constants between solution and solid-state environments produce band shifts; the apparent splitting of the lowest energy LMCT band shown by **3** and the resulting polychromism must consequently originate from differences in crystal packing between **2** and **3**. As noted above in the structural results section, **3**, in contrast to **2**, crystallizes as dimers, which exhibit considerable spatial overlap of the DHB^- units. In an attempt to account for the split LMCT absorption bands in **3** by computational means, a $(NH_3)_5Ru^{III}(DHB^-)$ dimer was constructed with maximum spatial overlap of the two DHB^- units and inversion symmetry (molecular point group C_i). The geometry of the dimer was optimized assuming that the two unpaired

(33) Shin, Y.-g. K.; Brunschwig, B. S.; Creutz, C.; Sutin, N. *J. Am. Chem. Soc.* **1995**, *117*, 8668–8669; and references cited therein.

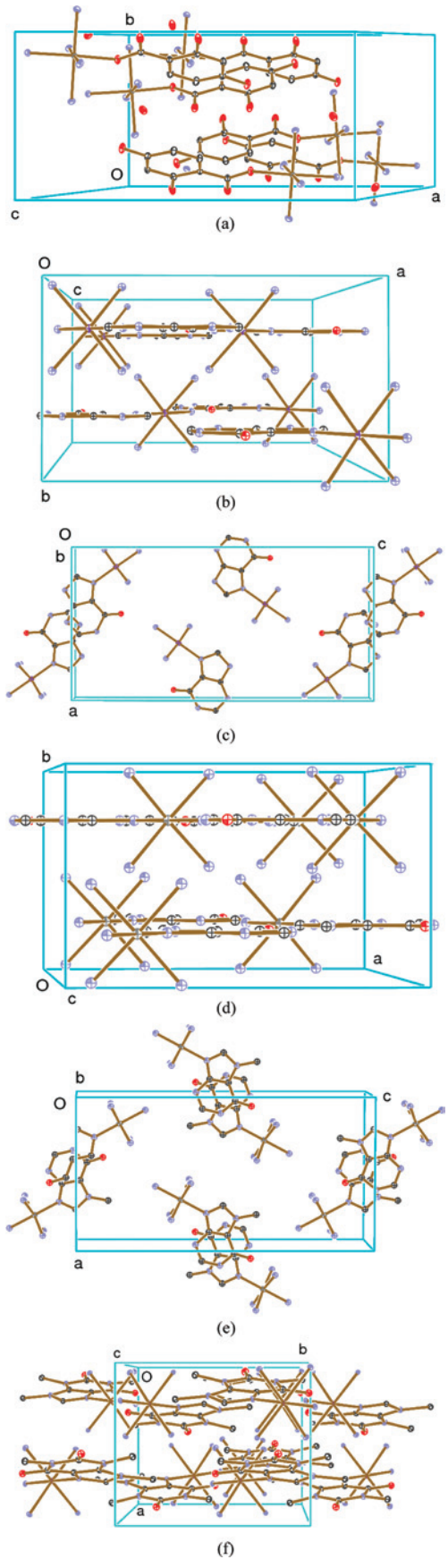

Figure 8. Partial packing diagrams of **3**, **4**, **5**, and **6** for use in the interpretation of their spectra: (a) **3** viewed along **c***; (b) **4** viewed along **c**; (c) **4** viewed along **b**; (d) **5** viewed along **c**; (e) **5** viewed along **b**; and (f) **6** viewed along **c**.

electrons, one on each Ru(III) ion, were triplet coupled to form a ^3A_u ground state. The optimized Ru−Ru distance in the computational dimer is 12.1 Å, while the experimentally determined Ru−Ru distance in **3** is 10.8 Å; the optimized distance between phenyl ring planes is 3.52 Å whereas the experimentally observed separation is 3.596(3) Å. Because DFT/B3LYP calculations do not include any treatment of dispersive interactions,[34] the good agreement nevertheless obtained between experimental and computed dimer geometries may indicate that the dominant interactions in the $\pi-\pi$ stacked dimer are electrostatic in nature.[34b]

The MOs of the dimer may be considered as in- and out-of-phase combinations of the individual $(NH_3)_5Ru^{III}(DHB^-)$ monomer orbitals. Thus, the partially filled Ru(d_{xz}) orbitals form new orbitals $D_{xz}^{\pm} = Ru_1(d_{xz}) \pm Ru_2(d_{xz})$, and the two highest doubly occupied orbitals combine into $\Pi^{\pm} = \pi(DHB_1^-) \pm \pi(DHB_2^-)$. The $D_{xz}^{\pm}$ orbitals are hardly split, as expected considering the large spatial separation between the two Ru centers; computed orbital energies of the two components, which contain one electron each in the dimer ground state, are $D_{xz}^-(a_g) = -3.27$ eV and $D_{xz}^+(a_u) = -3.28$ eV. However, the $\Pi^{\pm}$ orbitals are significantly split, since they are localized largely in the strongly overlapping phenyl moieties. The computed orbital energies of $\Pi^+(a_g)$ and $\Pi^-(a_u)$ are −6.78 and −7.23 eV, respectively. Two of the four possible elementary $\Pi \rightarrow D_{xz}$ excitations are forbidden by symmetry ($\Pi^+ \rightarrow D_{xz}^-$, $\Pi^- \rightarrow D_{xz}^+$). However, one allowed LMCT transition, which is predominantly the $\Pi^+ \rightarrow D_{xz}^+$ excitation, is computed at 19,400 cm^{-1} ($f = 0.074$); a second allowed LMCT transition, which is predominantly $\Pi^- \rightarrow D_{xz}^-$, is calculated at 24,000 cm^{-1} ($f = 0.008$). Relative to the LMCT transition calculated for the monomer in aqueous solution (~21,600 cm^{-1}), we compute a red-shift of 2,200 cm^{-1} for the first transition and a blue-shift of 2,400 cm^{-1} for the second transition. The transition energies computed from our model dimer match the polarized single crystal peak positions well (~20−21,000 cm^{-1} and ~24−25,000 cm^{-1}, Table 3).

We conclude that the crystal-packing arrangement in **3**, with its extensive spatial $\pi-\pi$ overlap between the DHB^- rings of adjacent $(NH_3)_5Ru^{III}(DHB^-)$ units, induces significant splitting among the π-type DHB^- orbitals in the ground state of the $(NH_3)_5Ru^{III}(DHB^-)$ dimers forming the unit cell of **3**. A spectroscopic consequence of this interaction is split LMCT excited states in **3** and a difference in color between crystalline **2** (yellow) and **3** (red). The TD-DFT calculations with modified B3LYP-type functionals predict a low-energy electronic spectrum containing two allowed transitions for the dimer. The good agreement obtained for the computed and experimental transition energies (Table 3) as well as the separation between the absorption peaks (~4,600 cm^{-1} computed, ~4,000 cm^{-1} observed) suggests that differential (excited vs ground state) dispersive interactions do not play a significant role in determining the positions of the LMCT states.

(34) (a) Kristyan, S.; Pulay, P. *Chem. Phys. Lett.* **1994**, *229*, 175. (b) Cybulski, S. M.; Seversen, C. E. *J. Chem. Phys.* **2005**, *122*, 014117–2946.

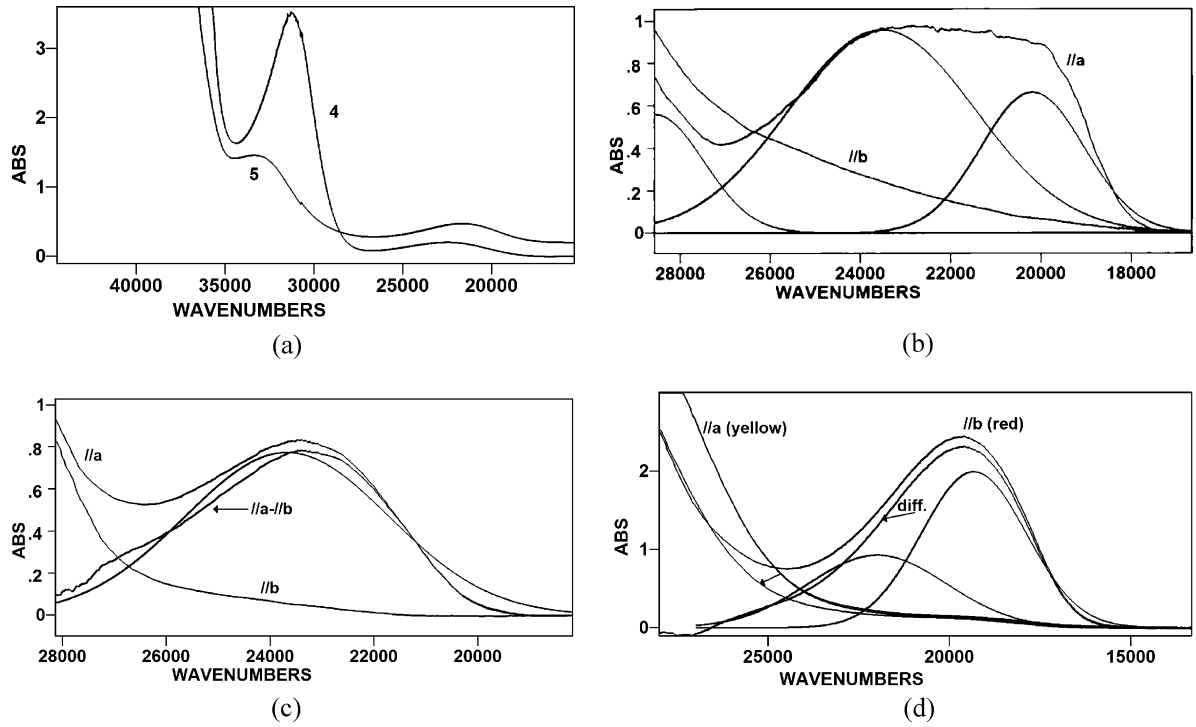

Figure 9. Electronic spectra and deconvoluted spectra of (a) 9.47×10^{-4} M **4** and 6.13×10^{-3} M **5** at room temperature in 50/50 H_2O/glycerol made 0.15 M in HCl. The path length was 0.15 cm in both cases; (b) 0.026 mm thick plate of **4** at room temperature with the absorption parallel to **a**, deconvoluted after subtracting the absorption parallel to **b** to correct approximately for the UV tail (the flattened absorption is not an artifact arising from stray light); (c) **5** at room temperature having a path length of 0.011 mm thick using a dummy band to approximate the UV tail for the deconvolution of absorption parallel to **a**; and (d) polarized spectra of **6** (path length 0.05 mm) at room temperature. Following subtraction of the red absorption UV tail (approximated by blue-shifting the yellow-polarized spectrum by 1400 cm^{-1}; see left arrow), the resulting "difference" visible spectrum was used for deconvolution.

Table 5. Summary of Observed (Deconvoluted) and Computed Electronic Spectra for Complexes **4**−**6**[a,b]

	solution			polarized single crystal			calc. (TD-DFT)		
system	energy	ε_{max}	$\Delta\nu^{1/2}$	energy	ε_{max}	$\Delta\nu^{1/2}$	energy	f	assignment
4	22,100	285	5,500	20,200	68[c]	2,700	22,300	$<10^{-3}$	O(n) → d(σ^*) LMCT
				23,500	98[c]	4,900	22,800	0.018	π → d_{xz} LMCT
	33,600	1,370	5,400				31,000	0.008	π → d_{xz} LMCT
							38,000	0.032	π → d_{xz} LMCT
5	23,000	141	5,800	23,300	188[c]	3,700	22,600	0.008	π → d_{xz} LMCT
	31,300	2,480	3,000				33,650	0.024	π → d_{xz} LMCT
							34,700	0.048	π → d_{xz} LMCT
6	19,600	310		19,300	125[d]	3,400	19,800	0.026	π → d_{xz} LMCT
				22,000	58[d]	4,500	22,100	$<10^{-3}$	O(n) → d(σ^*) LMCT
	32,400	1,330					28,100	0.011	π → π^*
							36,900	0.037	π → d_{xz} LMCT

[a] See Supporting Information for a more complete tabulation. [b] Energies in cm^{-1}; extinction coefficients (ε) in L mol^{-1} cm^{-1}. [c] Single-crystal, room-temperature, electric vector parallel to the **a** axis. [d] Single-crystal, room-temperature, electric vector parallel to the **b** axis.

PentammineRu^{III}(purine) complexes (4−6). Deconvoluted solution and single-crystal spectra of **4**−**6** are presented in Figure 9 and summarized in Table 5. Each complex consists of $(NH_3)_5Ru^{III}$ moieties bound to the imine nitrogen atoms of a purine ligand at either the N-7 (**4**, **6**) or N-9 (**5**) ring positions (Figure 1). Importantly, attachment of $(NH_3)_5$Ru(III) to imine nitrogen atom N-7 places a carbonyl oxygen atom of the planar purine ligand in a position to hydrogen-bond to two cis-oriented ammine groups.[14] In contrast, the sole carbonyl oxygen of the hypoxanthine ligand of **5** is well removed from possible intramolecular hydrogen bonding by attachment of $(NH_3)_5$Ru(III) to N-9; in this case, attachment of $(NH_3)_5$Ru(III) to N-7 is prohibited by methylation at that site.[14]

Solution spectra of **4**−**6** exhibit two relatively low-energy absorptions, which were assigned as purine → Ru(III) LMCT by Clarke and Taube.[14,35] Because quantification of the band widths observed for the solution absorptions was required for comparison to those observed in the single-crystal spectra, solution spectra of **4** and **5** were remeasured (Figure 9a), and they agree closely with the previously reported values.[35] The spectra measured in glassed solutions at 80 K (not shown) are little changed from those shown at room temperature, aside from modest band sharpening at the lower temperature. A striking feature shown by **4** and **6**, but not **5**, is that the lowest-energy absorption either is substantially broadened or clearly split in the solid-state spectra. Band widths of the apparently single visible absorptions shown, respectively, by solutions of **4** and **5** are presented in Table

(35) Clarke, M. J. *Inorg. Chem.* **1977**, *16*, 738–744.

5 for comparison with those determined from deconvolution of their single-crystal spectra.

Inspection of Figures 8b and 8d reveals that the electric vector of light polarized along the **b** axes of both **4** and **5** is perpendicular to the respective Ru−N(purine) bond vectors. However, the electric vector of light polarized along either their **a** or their **c** axes has a substantial component along the Ru−N(purine) bond vector, and this component is somewhat larger along **a** for **4** than **5** (Figures 8c and 8e); the difference is magnified in the calculated squares of these bond projections (Table 4). Thus, the low-energy absorptions shown by **4**, **5**, and **6** are strongly polarized along the Ru−N(purine) bond directions. The absorptions shown by **4** and **5** essentially vanish when the electric vector of polarized light is directed along their **b** axes, onto which the Ru−N(purine) bond vectors have zero projections. As is apparent from Figure 8f, the absorptions shown by **6** greatly diminish when the electric vector is rotated from **b** to **a**, a result which is consistent with the Ru−N(purine) bond projection decreasing from 0.884 to 0.098 (Table 4).

The more recent experimental results presented above support the prior assignment of these low-energy absorptions as purine → Ru(III) LMCT.[2,3] Moreover, as would be expected for LMCT, the low-energy absorptions shown by **6** are red-shifted with respect to those shown by **4** and **5** owing to the electron-donating property of the additional methyl groups present in **6** (Figure 1).

The electronically excited states of **4**−**6** were probed through TD-DFT calculations. For **5**, one low-lying purine(π) → Ru(d_{xz}) LMCT transition is predicted at 22,600 cm^{-1} (f = 0.008); to higher energy, two closely spaced intensity-carrying transitions are computed at 33,600 cm^{-1} (f = 0.024) and 34,500 cm^{-1} (f = 0.08). In solution, the bands observed for **5** (Table 5) are at 23,000 cm^{-1} and 31,300 cm^{-1}, respectively. The computed results for **4** present a similar pattern with a low energy LMCT absorption predicted at 22,800 cm^{-1} (f = 0.018), and two higher energy absorptions at 31,000 cm^{-1} (f = 0.008) and 38,000 cm^{-1} (f = 0.032). For **4**, the bands observed in solution (Table 5) peak at 22,100 cm^{-1} and 33,600 cm^{-1}, respectively. As mentioned above, the lowest-energy band of **4** is split in the crystalline phase (bands at 20,200 cm^{-1} and 23,500 cm^{-1}). Although the calculations on monomeric **4** do predict the presence of a second, low-energy excited state at 22,300 cm^{-1} (approximately 500 cm^{-1} *below* the intensity-carrying transition), the transition to this state carries insignificant oscillator strength ($f < 10^{-4}$). The calculations on **6** predict a purine(π) → Ru(d_{xz}) LMCT band at 19,800 cm^{-1} (f = 0.026), in excellent agreement with the solution spectral data (19,600 cm^{-1}, Table 5). The calculated value of ∼3,000 cm^{-1} for the methyl-group induced red-shift to the low-energy spectrum of **6** relative to **4** matches the experimentally observed value of ∼2,500 cm^{-1} well. To higher energy, the calculations predict a weak $\pi \rightarrow \pi^*$ transition at 28,100 cm^{-1} (f = 0.011), and a second LMCT transition at 36,900 cm^{-1} (f = 0.037). These two computed transitions flank an experimentally observed band peaking at 32,400 cm^{-1}. As with crystalline **4**, the lowest-energy band of **6** is split in the crystalline phase (bands at 19,300 cm^{-1} and 22,000 cm^{-1}) and, yet again, from the calculations on monomeric **6** there is no sign of a second, low-energy transition carrying measurable intensity. In the case of monomeric **6**, the transition computed closest in energy to the observed one is at *higher* energy and near-zero intensity (22,100 cm^{-1}, $f < 10^{-4}$). We shall return below to these two "silent" transitions in **4** and **6**.

We now briefly describe some of the causes we have considered to explain why the low-energy bands in crystalline **4** and **6**, but not in crystalline **5**, appear broad or split. In the published structures of **4** and **5**, and in the crystal structure reported here for **6**, the $(NH_3)_5$Ru(III)(xanthine) cations utilize crystallographic mirror planes, which contain the xanthine, the Ru(III) ion, and the N atom of the ammine trans to the xanthine ligand (molecular C_s point group symmetry). The crystal packing of **4** and **5** differs in that complex **4** enjoys considerably *less* purine π-stacking overlap than complex **5**.[3] When viewed along the **a** cell direction, **5** contains columns of pentammineRu(III)-hypoxanthine cations arranged centrosymmetrically, head-to-tail. In each column, the cations are equally spaced (3.41 Å interplanar spacing) and exhibit substantial overlap of the hypoxanthine units. In contrast to **3**, there are no dimeric units in **5**. This observation suggests that $\pi-\pi$ interactions are not responsible for the split electronic energy bands in **4** or in **6**. Indeed, in **6**, the xanthine-containing cations pack in a herringbone pattern with little indication of $\pi-\pi$ interactions. In **4**, the cations stack in an arrangement similar to that in **5**, but with substantially less overlap of their hypoxanthine rings, strongly suggesting that $\pi-\pi$ interactions are not responsible for the split electronic absorption band in the former system. Calculations in which weak purine−purine ring pi-overlap and interaction was simulated with the aid of an ethylenic species positioned above various purine C=C bonds did not produce any splitting in the low-energy purine−Ru band. The spectra of the $(NH_3)_5$Ru(III)(purine) complexes potentially contain n → π^* transitions of relatively low energy inherent to the purines, but these transitions have low intensity and are not observed as individual spectral features in solution. Importantly, the polarization of n → π^* transitions would be perpendicular to the purine plane and not in agreement with the observed polarization of the split bands: the **b** axes of **4** and **5** are perpendicular to the purine planes (Figure 8c,e), and the low-energy band(s) vanish for this polarization. Finally, the TD-DFT calculations position purine n → π^* transitions well above the observed bands in energy.

Next, we focused our attention on possible spectroscopic ramifications of the unique position occupied by one oxygen atom in complexes **4** and **6** vis-a-vis complex **5**. Hydrogen-bond interactions involving two ammines and the purine carbonyl groups of **4** and **6** position the carbonyl oxygen lone pair O(n) well for interaction with the Ru(III) ion (Ru−O ∼ 3.6 Å, Figure 2c). The ground-state configurations calculated by DFT for species **4** and **6** have, as expected, the d-electron vacancy in the Ru(d_{xz}) orbital ($^2A''$ state), and hence the potential O(n) → Ru(d_{xz}) LMCT transition would

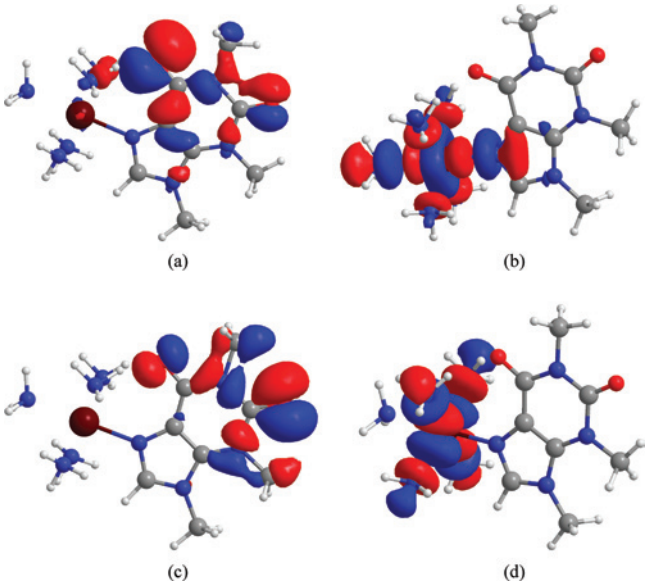

Figure 10. Contour plots of principal orbitals involved in the O(n) → Ru[d(σ*)] transition in **6**. The same isocontour value applies to all four plots. (a) HOMO-3 α spin−orbital, O(n); (b) LUMO α spin−orbital, Ru(d_{x^2}); (c) HOMO-2 β spin−orbital, O(n); and (d) LUMO+2 β spin−orbital, Ru($d_{y^2-z^2}$). The transition amplitudes for the elementary excitations HOMO-3 α → LUMO α and HOMO-2 β → LUMO+2 β are similar in magnitude and dominate the overall transition.

be weak for reasons of symmetry and would also be polarized perpendicular to the N(purine) → Ru axis. As discussed above, the real d-vacancy could contain (d_{xy}, d_{yz}) character because of spin−orbit mixing, but an electron occupancy change in the d-manifold to form a $^2A'$ reference ground state (i.e., the unpaired electron now resides in the (d_{xy}, d_{yz}) orbitals) in **4** or **6** leads to increases in total energy in both species, even after geometry reoptimization. Furthermore, TD-DFT calculations based on a $^2A'$ ground state do not predict any low-energy LMCT transitions with significant intensity, and two negative "d → d transition energies" (∼ −1000 cm^{-1}) emerge from these calculations. While intramolecular purine carbonyl interaction with Ru(d_{xy}, d_{yz}) orbitals could provide a first rationalization of the band broadening/splitting observed in the crystal spectra of **4** and **6**, the TD-DFT calculations also suggest that LMCT transitions of the type O(n) → Ru(d_{xy}, d_{yz}) carry negligible oscillator strengths and are well removed toward higher energy (>30,000 cm^{-1}). Thus, the DFT calculations strongly suggest that, in a one-electron picture, the ground states of **4**−**6** are best described as $^2A''$ states.

The DFT optimized structures of both **4** and **6** confirm the presence of two symmetric O−(H)N bonds in **4** and **6** with short interaction distances of about 1.87 Å; presumably, such O···H(N) interactions are disrupted for complexes **4** and **6** in aqueous solution. In both monomeric **4** and **6**, the "silent" transition mentioned above is of the LMCT type with proper *x*,*z*-polarization, and the excitation originates from the proximal oxygen lone pair, O(n); surprisingly, however, the transition terminates in formally antibonding Ru(III) d-orbitals of local σ-symmetry. The relevant donor/acceptor orbitals and elementary excitations are illustrated in Figure 10. We would tend to consider d(σ*) orbitals in near-octahedral $(NH_3)_5$Ru(III)−L type ligation as charge-transfer inactive in the visible-near UV region, because the octahedral t_{2g}−e_g* energy separation is large.[2,30] However, given the excellent spatial alignment of the O(n) donor orbital with the d(σ*) set of orbitals in **4** and in **6**, such LMCT excitations could potentially be of low energy. Careful examination of the data presented in Table 5 and Figure 9 indicates that the new band appearing in crystalline **4** grows in to the red of the solution band maximum, whereas the new band in crystalline **6** appears to be developing to the blue of the solution band. This is in full accord with the position in which the O(n) → d(σ*) transition is computed relative to the regular π(purine) → d_{xz} LMCT excitation (toward lower energy for **4**, higher energy for **6**; see above). Although the X-ray data obtained for **6** demands symmetry in the "heavy atom" skeleton, the hydrogen atoms were not located and their distribution need not be of the same symmetry as the crystalline environment.[36] To explore spectroscopic consequences of large amplitude motion, we arbitrarily placed one of the hydrogen atoms participating in O−(H)N bonding equidistant (∼ 1.40 Å) to N and O and recalculated the electronic transitions. This type of distortion increased the intensity of the O(n) → d(σ*) transition somewhat ($f \sim 10^{-4}$) without significantly changing the excitation energy. Small symmetry-destroying movements of the donor O-atom preferentially toward one of the hydrogen-bonding ammines also increased the transition intensity (to $f \sim 3 \times 10^{-4}$). Hence, we suggest that symmetry-destroying disorder associated with the O−(H)N bonds may provide the intensity mechanism for the proposed O(n) → d(σ*) transition.[37]

Solid-state spectroscopic oddities reported previously include the effects of conformational polymorphism,[38] allotropes showing different metal−ligand distances,[39] stacking changes which enable intermolecular charge-transfer absorptions,[40] and varying metal−metal distances shown by stacking of planar Pt(II) complexes.[41] The present study extends this list to include split LMCT bands arising from interionic π-stacking interactions of an aromatic donor ligand, as characterized in **3**. Although we offer a tentative assignment for the band broadening/splitting in crystalline **4** and **6**, the true origin of this observed solid-state effect on what appears to be purine → Ru(III) LMCT remains puzzling. We propose intra-ionic hydrogen bonding and local environmental asymmetry as a potential intensity-creating mechanism for the otherwise prohibitively weak LMCT transitions in crystalline **4** and **6**. In support of this suggestion, we note that hydrogen bonds are known to exhibit anomalous behavior. In the solid state, for example, asymmetric hydrogen bonds in a centrosymmetric environment have been observed,[36] while, with a second system, a distortion of local symmetry caused by dynamic hydrogen bonding effects was thought to be the

(36) Majerz, I.; Olovsson, I. *Acta Crystallogr.* **2007**, *B63*, 748–752.
(37) Calculations with added diffuse and polarization basis functions on O and on the hydrogens engaged in H-bonding also increase the intensity of the O(n) → d(σ*) transition slightly.
(38) Yu, L. *J. Phys. Chem. A* **2002**, *106*, 544–550.
(39) Bennett, M. J.; Donaldson, P. B. *Inorg. Chem.* **1977**, *16*, 655–660.
(40) Desiraju, G. R.; Paul, I. C.; Curtin, D. Y. *J. Am. Chem. Soc.* **1977**, *99*, 1594–1601.
(41) Connick, W. B.; Henling, L. M.; Marsh, R. E.; Gray, H. B. *Inorg. Chem.* **1996**, *35*, 6261–6265; and references cited therein.

cause of peak splitting in ^{13C}CPMAS spectra.[42] In solid tropolone, dynamic hydrogen bonds were shown to provide an efficient NMR relaxation mechanism,[43] while, with proton sponges, structural and NMR studies[44] suggest that asymmetric hydrogen bonding with a shallow double-minimum potential well is the norm for these systems.

Conclusions

The $(NH_3)_5Ru^{III}(L)$ cations in the structures of **2**−**6** all exhibit slight deviations from octahedral symmetry, a staggered orientation of the nearly planar or planar ligands L with respect to the equatorial ammines, and the presence of intraionic N−H···X(ligand) hydrogen bonds when L contains an appropriate acceptor. Differences among the crystals include varying amounts of hydrogen bonding and $\pi-\pi$ stacking. The yellow (**2**) and red (**3**) forms of $(NH_3)_5Ru^{III}(DHB^-)SO_4\cdot$solvate yield identical solution spectra; hence, their different colors are attributed to differences in crystal packing. In particular, in contrast to **2**, **3** forms centrosymmetric cation dimers which exhibit extensive $\pi-\pi$ overlap. Calculated (TD-DFT) energies and oscillator strengths of the $\pi \rightarrow \pi^*$ and $\pi \rightarrow d_{xz}$ LMCT absorptions in the UV−vis spectral regions for **1** (DHB^-) and **2** agree well with the experimental values obtained from the deconvoluted solution spectra. Good agreement is also obtained for the single-crystal spectrum of **3**, in which extensive $\pi-\pi$ overlap between the DHB^- rings of adjacent $(NH_3)_5Ru^{III}(DHB^-)$ units induces significant splitting of the π-type orbitals in the ground state and accounts for the observed split LMCT excited states. The polarizations and energies of the broad/split visible absorptions shown by **4** and **6** also suggest assignment as LMCT. Complex **5** did not exhibit either split visible absorptions or the intramolecular N−H···O(carbonyl) hydrogen bonding observed for **4** and **6**. In contrast to **2** and **3**, none of the complexes **4**−**6** form dimers in the solid state, and the present study does not afford computational support relating the split absorptions in crystalline **4** and **6** to the details of $\pi-\pi$ purine overlap. TD-DFT calculations suggest that the additional bands observed for crystalline **4** and **6** may be O(n) → d(σ^*) LMCT in nature with absorption intensity gained from the presence of intraionic hydrogen bonding. However, the computed overall weakness of these transitions is of significant concern, and the assignment should thus be considered tentative.

Acknowledgment. We thank the reviewers for thoughtful comments, which helped us improve the manuscript. The present work elaborates on some of the pioneering studies of Ru(III) charge-transfer absorptions from the laboratory of the late Professor Henry Taube and is dedicated to his memory.

Supporting Information Available: Crystallographic details, including hydrogen bond data, in CIF format for the three structures described in the manuscript; crystallographic details in CIF format for the room-temperature structures of **2** and **3**; complete ref 19; DFT optimized geometries and TD-DFT excited-state data for **2**−**6**. This material is available free of charge via the Internet at http://pubs.acs.org.

IC800511G

(42) Khan, M.; Brunklaus, G.; Enkelmann, V.; Spiess, H.-W. *J. Am. Chem. Soc.* **2008**, *130*, 1741–1748.
(43) Detken, A.; Zimmermann, H.; Haeberlen, U.; Luz, Z. *J. Magn. Reson.* **1997**, *126*, 95–102.
(44) Stibrany, R. T.; Schugar, H, J.; Potenza, J. A. *Acta Crystallogr.* **2002**, *E58*, o1142–o1144; and references cited therein.